CEAS-GNC-2024-040

EuroGNC Navigation Guidance Control CEAS Bristol, UK June 11th-13th 2024
University of BRISTOL ROYAL AERONAUTICAL SOCIETY AIAA

Flight Control Law Design using H_∞ optimal control for Gust Load Alleviation of Flexible Aircraft

Abdelmoez Elagroudy Research Associate, German Aerospace Center (DLR), Institute of System Dynamics and Control, 82234, Oberpfaffenhofen, Germany. elagroudy94@gmail.com

Christian Weiser Research Associate, German Aerospace Center (DLR), Institute of System Dynamics and Control, 82234, Oberpfaffenhofen, Germany. christian.weiser@dlr.de

Simon Schulz Research Associate, German Aerospace Center (DLR), Institute of System Dynamics and Control, 82234, Oberpfaffenhofen, Germany. simon.schulz@dlr.de

Jan Tilmans Research Associate, RWTH Aachen University, Institute of Flight System Dynamics, 52062, Aachen, Germany. tilmans@fsd.rwth-aachen.de

ABSTRACT

This paper presents the design of a gust load alleviation control law for a transport aircraft, represented by a dynamic flexible model. The control law reduces the structural loads and thus helps to decrease the aircraft's structural weight. For the gust alleviation control, a linear full-order state-space controller is designed based on the H_∞ optimal control method. The control law design uses an accelerometer on the wing tip as a sensor and controls the outboard ailerons to alleviate the structural loads, in particular the wing root bending moment. The controller's load reduction performance is evaluated by simulating aircraft response to different vertical discrete gusts and the robustness is assessed by considering the worst-case combination of gain and phase errors. Finally, the load reduction performance is investigated for different actuator deflection rate limits, and the complete strategy for load alleviation using sensors on the wing tips is assessed.

Keywords: Flight Control Law Design; Flexible Aircraft; Gust Load Alleviation; H_∞ Control; Robust Control; Optimal Control; Actuator limitations

Nomenclature

$\mathbf{V}_b$	=	Translational velocity of rigid body, body-fixed coordinates
$\mathbf{\Omega}_b$	=	Angular velocity of rigid body, body-fixed coordinates
$\mathbf{u}_f$	=	Modal deformations
$\mathbf{M}_{ff}$	=	Mass matrix
$\mathbf{B}_{ff}$	=	Damping matrix
$\mathbf{K}_{ff}$	=	Stiffness matrix
$\mathbf{P}_g^{\text{ext}}$	=	External loads
$\mathbf{P}_g^{\text{aero}}$	=	Aerodynamic loads
$\mathbf{P}_g^{\text{dist}}$	=	Aerodynamic disturbance loads
$\mathbf{P}_g^{\text{prop}}$	=	Propulsion loads
$\mathbf{P}_c$	=	Internal cut loads

δ	=	Control surface deflection
M_x	=	Wing bending moment
M_y	=	Wing torsion moment
a_f	=	Vertical acceleration, sensor signal
w_{gust}	=	Gust velocity
H	=	Gust gradient
U_{ds}	=	Gust amplitude
s	=	Laplace operator in frequency domain
ω_0	=	Natural frequency
ξ	=	Damping ratio
P_{M_x}	=	Total load reduction index, bending moment
Index g	=	Structural grid coordinate
Index b	=	Rigid modal coordinate
Index f	=	Flexible modal coordinate
Index j	=	Aerodynamic panels coordinate
Index wr	=	Wing root
Index wt	=	Wing tip

1 Introduction

In the design process of new aircraft, one of the major goals is to reduce the exhaust emissions. Another economical goal is to reduce operational costs. Fuel consumption represents a large share of direct operating costs. For example, for a medium range Airbus A330, fuel cost can represent up to 25% of the direct operating costs depending on the fuel prices [1]. These goals can be achieved directly by reducing aircraft weight. The aircraft experiences external structural loads from different sources during flight as well as on the ground: engines' thrust, aerodynamic lift & drag, gravity and ground (landing gear) loads [2]. These result in external loads on the aircraft structure, and lead to, in general elastic, elongation and compression of the aircraft structures [2]. For higher loads, which exceed the design limits, the material can experience plastic deformation or even material failure. In order to withstand these loads, mechanical stresses on the material need to be lower than the material strength limits. To ensure this, critical locations on the aircraft, which are subject to high loads, need to be reinforced with structural supports or to have a higher thickness.

In order to build a lighter aircraft's structure there are, among others, two main approaches. The first approach is to save structural weight by using lighter advanced materials like carbon fiber composites, which have small density and can withstand relatively high structural stresses like metal alloys. The second approach is to ensure that structural loads are limited within acceptable range using load control. Unanticipated atmospheric disturbances, like discrete gusts, put strain on structures that interact the most with airflow, such as wings and tailplane. The determinant factor which rule the structure mass, are the critical load cases caused by gusts or flight maneuvers [3]. In [4], using the example of a 200-seater aircraft, it is shown that gust loads can exceed maneuvering loads and create the most critical load cases. The simulation result of this work shows that the wing root bending moment reaches a peak value equal to 1.8 of the nominal value at normal cruise condition, due to a discrete gust.

By deflecting flight control surfaces, the aerodynamic forces and moments can be shaped. For example, multiple ailerons can be used to change the lift distribution over the wing. Moreover, during a vertical discrete gust, deflecting the ailerons symmetrically upward, reduces the lift forces locally and concentrates them in the innermost part of the wings, which reduces the integrated loads at the wing root. Another strategy for gust load alleviation is to keep the same angle of attack and reduce the influence of wind by changing the aircraft attitude according to the atmospheric disturbance [5]. The use of gust

load control enables a reduction in aircraft weight, resulting in lower fuel consumption. Furthermore, mitigating wing root loads, makes it possible to increase the wing aspect ratio, which leads to less induced drag, and thus less required thrust force and fuel. Due to the fast dynamics of some aerodynamic disturbances, the effectiveness of a gust load alleviation system can be fundamentally constrained by sensor and actuator bandwidths [6]. In other words, actuators and sensors need to have the ability to respond quickly to high frequency gusts. With a cruising speed of 250 m/s aircraft passes through most of the design-relevant gusts in less than 1 second.

The main contribution of this work lies in calculating how much total load reduction is achievable given a specific deflection rate limit of the actuators. This work also demonstrates that the feedback control strategy, using accelerometers on the wing tip, has inherent physical limitations, and expects that the total load reduction with this strategy will not exceed 33%, regardless of the actuator speed. Additionally, this paper presents a possible approach to tune and design a robust control law for gust load alleviation using H_∞ optimal control.

This paper is structured in five sections including the current introduction and a section for conclusion. Section 1.1 explores previous works related to Gust Load Alleviation (GLA), section 2 presents the linear flexible aircraft model utilized in this work. In Section 3, a brief introduction to the H_∞ optimal control theory is provided, the GLA optimization problem is defined, and the synthesis process is described. Finally, the robust stability of the closed-loop system is assessed. In Section 4, the GLA controller's performance is evaluated concerning the defined design requirements. At the end, a parameter study is conducted to investigate all possible load reduction potentials for different actuator limitations.

1.1 State of the Art

For gust load alleviation, different sensors and controller design approaches have been studied or tested in flight in previous works. In this section, some of these sensors and design strategies are discussed.

1.1.1 Sensors

There are mainly two different strategies which can be used for GLA. The first strategy focuses on capturing the dynamics or movement of an aircraft's response to a discrete gust or - in general - to an aerodynamic disturbance. This approach is simple, widely used, and has been tested in flight many times [7–10]. However, the disadvantage of this approach is that the controller cannot act before the structure starts to move. As a result, the command signal is always reactive rather than proactive, which can pose a challenge for the actuators, which need to respond quickly to limit the extra loads generated. The second strategy aims to address the limitations of the first approach by detecting the aerodynamic disturbance before it reaches the aircraft, thereby allowing the actuator sufficient time to respond. Acceleration sensors or accelerometers belong to the first strategy and are the most commonly used sensors for gust load alleviation. As the name indicates, accelerometers provide inertial acceleration components in the three dimensional space. For GLA systems it can be mounted on the wing [7] or on the front part of aircraft fuselage [11], in order to give the actuators adequate time to respond. Airbus A320 implemented a GLA system using accelerometers located ahead of the wings along the fuselage, in order to compensate the lag of the hydraulic actuators [11]. Since an aircraft wing has a free end, wing-accelerometers are usually placed at the wing tip because the dynamics of the gust response are clearly visible at this point.

For the second strategy, a Light Detection And Ranging (LIDAR) sensor has been developed within the European project AWIATOR to capture aerodynamic disturbance before it reaches the aircraft. The airborne turbulence LIDAR sensor uses short-pulse ultraviolet waves and can measure air flow within a range of 50 to 150 meters [12]. In 2004, the first flight test of the LIDAR system was performed using the DLR ATTAS test aircraft [12]. Later, the system was successfully applied to an Airbus A340 and was able to measure vertical gust speed in front of the aircraft [13, 14]. Many GLA systems have

used this - relatively new - LIDAR technology in the control law design process [5, 15]. Assuming a perfect gust signal can be measured via the LIDAR sensor, an adaptive feedforward GLA system has been developed and tested on a flight dynamics model for McDonnell Douglas F/A-18 Hornet aircraft [16]. Air data sensors, which belong to the same strategy as LIDAR, use static pressure ports to detect aerodynamic disturbances before they reach the aircraft's wing. The sensors, however, are limited to measuring gusts only at their specific installation location, in contrast to the more flexible measurement capability of LIDAR. These pressure ports can detect gust perturbations from changes in the aircraft's angle of attack, and are often placed at the nose of the aircraft, in an attempt to compensate for time delays of actuators[15]. Static air data sensors have been applied in several aircraft systems for gust load alleviation. For example, the Boeing 787 uses these sensors to detect the onset of lateral and vertical turbulence for a flying quality enhancement system [17]. The Northrop Grumman B-2 uses similar sensors in its gust load alleviation system [17].

1.1.2 Control Law Design for Gust Load Alleviation

Depending on the used sensors, two different control strategies can be used for GLA.The first design strategy is to use measurements from aircraft response to gust, and send a feedback control command, see e.g. [18–20]. This design approach use mainly accelerometers and gyroscopes to measure vertical load factor and pitch rate [5].This strategy allows designing of the closed loop poles, and ensuring stability and robustness to system uncertainties, without the need to know the exact model of the aircraft. The second strategy measures wind perturbation and sends a feedforward command, to prevent the aircraft response before it starts to move [21]. The second approach uses - in most cases - LIDAR measurements which can capture vertical and lateral gusts in front of the aircraft. In order to improve loads reduction, a mixed feedback/feedforward control approach has been investigated in previous works [22, 23].

2 Aeroelastic Aircraft Model

The first step to design a GLA control law is to accurately model the aeroelastic aircraft's dynamic behavior and response to gusts. Although building such a model can be the sole objective of a separate study [24], this section provides a brief overview of the utilized aeroelastic model, since the main focus of present work is on designing the GLA control law. The model represents a generic commercial aircraft derived using "Variable Loads Environment" (Varloads) framework [25].

2.1 Equations of Motion & Aerodynamics

The first simple idea to model an aircraft, is to treat it as a rigid body, neglecting its flexible properties that arise from the elastic nature of its structure. Aircraft flexibility could be taken into consideration by modeling it using a number of discrete mass points. These discrete mass points, or lumped masses, can be constructed by reducing a Finite Element Model (FEM) of the aircraft [25], and allow for each mass point to have additional six degrees of freedom. The mass points are located in the nodes of a structure grid. The structure grid nodes, are connected to each other by stiffness & damping matrices [2]. These matrices represent the structure properties and determine the deformation shape resulting from external forces. This approach results in a fully flexible structure, allowing for more accurate modeling of aeroelasticity by using the deformed structure to calculate the aerodynamic loads.

The following equations of motion describe the dynamics of the flexible aircraft [26]:

$$\begin{aligned} \begin{bmatrix} \mathbf{M}_b \left(\dot{\mathbf{V}}_b + \boldsymbol{\Omega}_b \times \mathbf{V_b} - \mathbf{T}_{bE} \cdot \mathbf{g}_E \right) \\ \mathbf{J}_b \, \dot{\boldsymbol{\Omega}}_b + \boldsymbol{\Omega}_b \times (\mathbf{J}_b \, \boldsymbol{\Omega}_b) \end{bmatrix} &= \boldsymbol{\Phi}_{gb}^T \, \mathbf{P}_g^{\text{ext}} \\ \mathbf{M}_{ff} \, \ddot{\mathbf{u}}_f + \mathbf{B}_{ff} \, \dot{\mathbf{u}}_f + \mathbf{K}_{ff} \, \mathbf{u}_f &= \boldsymbol{\Phi}_{gf}^T \, \mathbf{P}_g^{\text{ext}} \quad . \end{aligned} \tag{1}$$

The first equation represents the rigid body dynamics, which are described by the non-linear Newton-Euler equations of motion. In this equation, $\mathbf{V}_b = [u_b\ v_b\ w_b]$ and $\mathbf{\Omega}_b = [p_b\ q_b\ r_b]$ are the linear and angular velocity components of the aircraft (i.e., the rigid body states). The index b indicates a notation in the body-fixed frame, which rotates with the aircraft's center of mass. $\mathbf{M}_b$ and $\mathbf{J}_b$ are the mass and inertia tensors of the aircraft in body coordinates. The vector $\mathbf{g}_E = [0\ 0\ -g]^T$ denotes the gravity vector in earth-fixed coordinates and $\mathbf{P^{ext}}_g$ denote the external forces, which consist of aerodynamic $\mathbf{P}_g^{\text{aero}}$ and propulsion loads $\mathbf{P}_g^{\text{prop}}$. The second equation represents the flexible structural dynamics as a second-order differential equation, where $\mathbf{u}_f$ represents the modal deformations (and its derivative, modal velocities, and second derivative, modal accelerations. The modal structural dynamics are determined by the mass $\mathbf{M}_{ff}$, damping $\mathbf{B}_{ff}$, and stiffness $\mathbf{K}_{ff}$ matrices in modal coordinates (index f). Again, $\mathbf{P}_g^{\text{ext}}$ represents the external loads applied on the nodes of the structural grid (index g). $\mathbf{\Phi}_{gb}$ and $\mathbf{\Phi}_{gf}$ are the transformation matrices from the (rigid and flexible) modal coordinates to the structural grid coordinates. To obtain the internal loads [2], also known as cut loads $\mathbf{P}_c$, the total nodal loads need to be transformed with a transformation matrix into the cut-loads coordinate system (index c). The nodal loads can be calculated from the external loads and the inertial loads. More details about the calculation of cut loads $\mathbf{P}_c$ can be found in [26, 27].

While the $\mathbf{P}_g^{\text{prop}}$ is usually fixed at the defined operating point, the aerodynamic loads $\mathbf{P}_g^{\text{aero}}$ are variable and depend on many variables, including the shape of the deformed structure. To be able to model this aeroelastic effect, the aircraft surface is modeled using aerodynamic panels. These panels can change their position and orientation, depending on the movement and rotation of the structure nodes. Figure 1 shows the aerodynamic panels used to calculate the aerodynamic forces. Using the Doublet Lattice Method (DLM), the unsteady aerodynamic loads on the aerodynamic panels can be calculated as follows [26]:

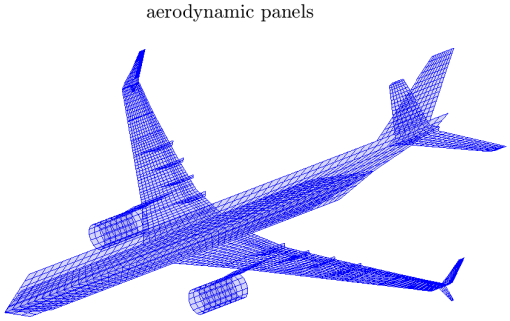

Fig. 1 Aircraft lifting surface split into finite number of aerodynamic panels

$$P_g^{\text{aero}} = q_\infty\, T_{kg}^T\, S_{kj}\, \Delta c_{p_j}(k)\ , \tag{2}$$

where q_∞ is the free-stream dynamic pressure, S_{kj} is the area of each panel, j is the panel index, and $\Delta c_p j(k)$ is the difference in pressure coefficients over each panel, which is a function of k, the reduced frequency [28]. To calculate the aerodynamic loads, the DLM requires the velocities $w_{\text{dist,j}}$ and accelerations $\dot{w}_{\text{dist,j}}$ of the wind disturbance at each panel [28]. For more detailed information about this point, the reader is referred to [26, 28, 29].

2.2 Actuator Model

Given the high dynamics of gusts, the dynamics of the actuator play a crucial role in the design of a GLA controller. The actuator dynamics vary based on the device, however, typical values for transportation aircraft can be found in the literature [5]. The dynamics of the actuator can be modeled by a second-order low-pass filter as follows:

$$G(s) = \frac{\omega_0^2}{s^2 + 2\,\xi\,\omega_0\,s + \omega_0^2}\ . \tag{3}$$

The cutoff frequency ω_0 represents the frequency at which the magnitude of an actuator's output drops to approximately 70% of the input signal's amplitude. This corresponds to a gain of -3 dB in the frequency response diagram. In other words, the cutoff frequency is the point at which an actuator begins to attenuate an input signal. Although the linear model approximates the system's dynamic behavior, it does not account for nonlinear effects such as saturation. However, the controller synthesis must consider the actuator's capabilities and limitation, such as the maximum deflection angle and deflection rate. Table 1 shows the numerical values used for the actuator model and for the controller synthesis [5].

The linear model is now available for designing the control law and performing subsequent simulations. For simplicity, we will refer to this model as the Flexible Aircraft Model (FAM) for the control law design.

Quantity	Symbol	Value
Actuator cutoff frequency	ω_0	4 Hz
Actuator damping ratio	ξ	0.85
Maximum deflection angle	$\delta_{\max}$	30°
Maximum deflection rate	$\dot{\delta}_{\max}$	40°/s

Table 1 Numerical values of the actuator model[5]

2.3 Gust Model

The simulations in this study focus on the certification process of commercial aircraft. Airworthiness authorities have established standard wind disturbance models as a certification requirement for large commercial aircraft to ensure their safety. These models are specified in the European Aviation Safety Agency Certification Specifications (EASA CS-25) [30]. A discrete gust, as defined in CS-25.341, can be described with the following equation:

$$w_{gust} = \frac{U_{ds}}{2}\left(1 - \cos\left(\frac{\pi x}{H}\right)\right) \quad . \tag{4}$$

The discrete gust is defined within the range of $0 \leq x \leq 2H$, where w_{gust} represents the wind velocity, U_{ds} represents the maximum amplitude of the gust and H is the gust gradient and represents half of the gust's width. Figure 2 shows an example of a vertical discrete gust with H = 80 m and U_{ds} = 16 m/s. Table 1 presents the numerical values of the gust model used for the simulations. The gust gradient range is defined according to the certification requirements CS-25, while the gust amplitude is fixed, deviating from CS-25.341.

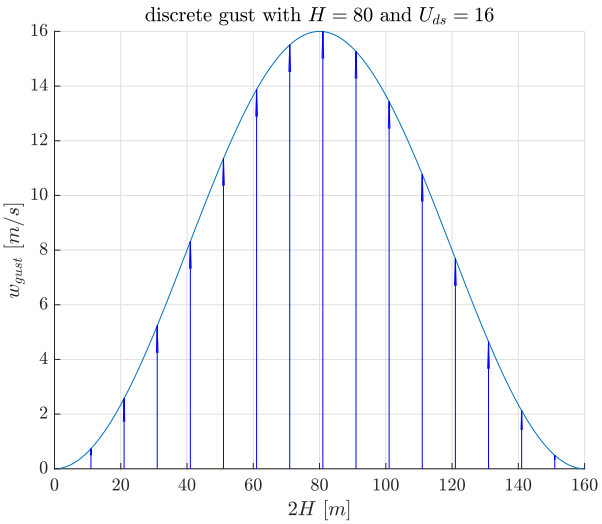

Fig. 2 Example for a discrete gust

Quantity	Symbol	Value
Gust amplitude	U_{ds}	15.598 m/s
Gust gradient	H	[9 – 107] m

Table 2 Numerical values of the discrete gusts used in the simulations

3 Control Law Design

Given the advantages of H_∞ control [31], H_∞ optimal control is used to synthesize the GLA controller, based on the linear model defined in the previous section. In this section, a brief overview of the used H_∞ control technique is given, the GLA optimization problem is defined, and the synthesis process is described. Finally, the stability of the closed loop is investigated.

The design of the control law is performed at a single operating point, where the nonlinear model is linearized. This operating point is defined by a Mach number of 0.85 and an altitude of 10,668 meters and represents a typical cruise flight conditions. The design objectives of the control law are as follows:

- Minimize the additional bending moment load at the wing root caused by discrete vertical gusts. This requirement is the primary goal of the system and of this work. Reducing bending moment loads at the wing root represents the typical design goal for gust load alleviation systems [5].
- Ensure that the control signals fall within the defined range and limits of the actuator, as presented in Table 1. These values represent the typical values for commercial aircraft, and have been used to design a gust load alleviation controller in [5].
- Ensure closed-loop stability with a gain margin of 7 dB and a phase margin of 60°. These values are more conservative than standard stability margins requirements, since parametric uncertainty is not considered in the model (standard: gain margin > 6dB, phase margin > 45° [32]).

The first step in designing a GLA controller is to choose the control surfaces and sensors used for measuring feedback signals. The simplest approach to control law design is to use a Single Input Single Output (SISO) system. To this end, a single accelerometer sensor is placed at each wing tip, where the movement of the wing can be observed. The vertical component of the sensor signal $a_{f,wt}$ is used as the feedback signal. As for the control signal, the four outboard ailerons move together and symmetrically on both sides, representing a single control signal δ. These control surfaces are located away from the wing root, can move in both directions, and typically have actuators with higher deflection rates than other control surfaces. These properties are positively valued.

3.1 H_∞ Optimal Control Theory

The H_∞ optimal control theory aims to find the optimal control law by solving an optimization problem. A general formulation of parameter optimization problems is given by [33]:

$$\min_{x \in \mathbb{R}} \; J(x) \; . \tag{5}$$

In this equation, $J(x)$ is the cost function, also called objective function and x represents the optimization variable. The optimization problem is described as follows: find a value for the optimization variable $x \in \mathbb{R}$ which minimizes the cost function $J(x)$. The cost function output is a scalar value, and represents the total penalty or cost, which needs to be minimized. The solution of the optimization problem is denoted $x_{optimal}$. In H_∞ optimal control theory, the controller K is the optimization variable, and the optimizer searches for the optimal controller $K_{optimal}$.

The general formulation of the control loop is illustrated in Figure 3, where P is the generalized plant, K is the controller, u is the control command, v is the measured output, w represents external inputs, such as disturbances, and z is the regulated output, or the error signal, which is minimized to achieve the control objectives [31].

Applying this theory to the current GLA setup, P is the FAM with weighting functions, u represents the control command δ, v represents the acceleration $a_{f,wt}$, w represents the gust signal w_{dist}, and z is a vector that includes $M_{x,wr}$, the bending moment, and δ, the control command. Equation 6 gives the system behavior from disturbances to regulated outputs, where $F_l(P, K)$ is the closed-loop transfer

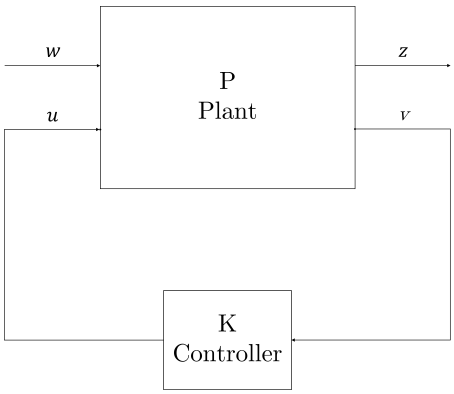

Fig. 3 General formulation of the H_∞ optimal control

function from w to z.

$$z = F_l(P, K)\ w\ . \tag{6}$$

The optimization problem to be solved is to find the stabilizing controller K that minimizes $|F_l(P, K)|_\infty$:

$$\min_K\ \|F_l(P, K)\|_\infty \tag{7}$$

$\|F_l(P, K)\|_\infty$, the infinity norm of the closed loop $F_l(P, K)$ from w to z, has several performance interpretations [31]. In the time domain, $\|F_l(P, K)\|_\infty$ is the maximum ratio of the 2-norm of the output signal $z(t)$ to the 2-norm of the input signal $w(t)$ for non-zero $w(t)$ [31]:

$$\|F_l(P, K)\|_\infty = \max_{w(t)\neq 0} \frac{\|z(t)\|_2}{\|w(t)\|_2} = \max_{\|w(t)\|_2=1} \|z(t)\|_2 \tag{8}$$

where $\|z(t)\|_2 = \sqrt{\int_0^\infty \Sigma_i\ |z_i(t)|^2\ dt}$ is the 2-norm of the vector signal.

To understand the interpretation of $\|F_l(P, K)\|_\infty$ in the frequency domain, the frequency response from w to z is considered. Let $z(\omega)$ denote the response of a system to a permanent sinusoidal input $w(\omega)$. Then $z(\omega) = G(j\omega)\ w(\omega)$, where $G(j\omega) = F_l(P, K)(j\omega)$ is frequency response from w to z. In the frequency domain, $\|F_l(P, K)\|_\infty$ is the maximum value of $\overline{\sigma}(F_l(P, K)(j\omega))$ over all frequencies ω [31]:

$$\|F_l(P, K)(s)\|_\infty = \max_\omega \overline{\sigma}(F_l(P, K)(j\omega)) \tag{9}$$

where $\overline{\sigma}(F_l(P, K)(j\omega))$ is the maximum singular value of $F_l(P, K)(j\omega)$. For a given frequency ω, the maximum singular value $\overline{\sigma}(G(j\omega))$ is defined as follows [31]:

$$\overline{\sigma}(G(j\omega)) = \max_{w(\omega)\neq 0} \frac{\|z(\omega)\|_2}{\|w(\omega)\|_2} \overset{\|w(\omega)\|_2=1}{=} \max_\omega \|z(\omega)\|_2\ . \tag{10}$$

For a SISO system $G(s)$, the singular values over all frequencies converted to decibel (dB) is identical to the magnitude of the Bode diagram of $G(s)$. Using the definition of $\overline{\sigma}(G(j\omega))$ in equation 9 yields:

$$\|F_l(P, K)(s)\|_\infty \overset{\|w(\omega)\|_2=1}{=} \max_\omega \|z(\omega)\|_2 \tag{11}$$

where:

$$\max_\omega \max_\omega \equiv \max_\omega\ . \tag{12}$$

Considering the two-dimensional vector $\vec{z(s)} = (z_1(s), z_2(s))$, the minimization problem in the frequency domain, for a normalized sinusoidal disturbance input $\|w\|_2 = 1$ with variable frequency and amplitude

of one, is given by the following equation:

$$\min_{K} \quad \max_{\omega} \left(\sqrt{|z_1(j\omega)|^2 + |z_2(j\omega)|^2} \right) \quad . \tag{13}$$

The optimization problem searches for the optimal controller K, which minimizes the maximum value of the term under the root, over all input frequencies. Let $G_{z_i w}$ denote the closed-loop transfer function from w to z_i. Here, $|z_i(j\omega)|^2$ is the magnitude squared of the frequency response, and it is identical with the squared magnitude of the Bode diagram of $G_{z_i w}$.

The solution of the optimization delivers the optimal controller $K_{optimal}$. However, finding the optimal controller can be computationally expensive, so a suboptimal solution $\gamma > \gamma_{min}$ is often sufficient to satisfy the optimization objectives:

$$\|F_l(P, K)\|_\infty < \gamma \quad . \tag{14}$$

This can be achieved by reducing γ iteratively. More details about the iterative minimization algorithm can be found in [31, 34].

3.1.1 H_∞ Controller Types and Model Reduction

The controller K can be classified into two categories: full order state-space controllers and controllers with a fixed control structure and variable parameters. The H_∞ optimal control problem can address both types of controllers.

In the structured H_∞ control problem, the designer can select the controller structure and a predetermined number of tunable gains and filters, such as a simple PID controller. The optimizer then finds an optimal solution, determining the numerical values of these tunable parameters. This design approach is straightforward and typically requires less computational power during flight, especially for a few tunable variables [35]. However, the main drawback of the structured H_∞ approach is that its associated optimization problem is based on non-smooth, non-convex optimization [35]. Non-convex optimization means that the problem has more than one minimum: a global minimum and at least one local minimum [33, 36]. Non-convexity can result in the solution converging to a local minimum with poor performance. Thus, the final solution is significantly influenced by the choice of the controller structure, the number of tunable parameters, and their initial guesses. As a result, the structured H_∞ approach is often plagued by the problem of non-repeatability [35]. On the other hand, classical H_∞ optimal control uses a full-order state-space controller with the same number of states as the generalized plant P as optimization variables [31]. The optimizer searches for an optimal solution of the matrices' elements A, B, C, and D. The optimization problem can be formulated as a convex problem [37], leading to a unique optimal solution. This solves the non-repeatability issue of the structured H_∞ approach. Another advantage of the state-space controllers is that there is no need to allocate specific sensor signals to control signals or to define a specific control structure [5], as the optimal control allocation is directly part of the optimization process. With more optimization variables and degrees of freedom, the full-order state space controller makes the best use of the full frequency content of complex aeroelastic models [5].

Given these advantages, a full-order state space controller has been used in the current work. However, the available aeroelastic model (FAM) introduced in the last section has 1600 states. A full-order state space controller for the original model would be computationally expensive in the optimization process as well as during flight. Therefore, a model reduction was conducted using MATLAB's function "balred" to create a reduced order model of the FAM with 160 states, which is used for controller synthesis [38]. Nevertheless, the full-order model has been used in the simulations and analysis.

3.2 Control Synthesis

As a design requirement,the GLA controller must be able to mitigate bending moment loads at the wing root while considering actuator limitations. To achieve this, the regulated output signal z must include the wing root bending moment $M_{x,wr}$ and the control signals δ. The optimizer minimizes the infinity norm of z, also known as the cost function [33], based on an external disturbance w with a variable frequency, where $|w|_2 = 1$. Figure 4 shows the optimization setup for the GLA problem. $G(s)$ represents the reduced order FAM model, $K(s)$ represents the state space controller to be optimized with 160 states, the same size as $G(s)$, and W_w, W_δ, and W_δ are weighting functions. As the disturbance signal w is normalized ($|w|_2 = 1$), the function W_w scales the input signal with the expected gust amplitude considered by the design:

$$W_w = U_{ds} \ . \tag{15}$$

Also, $M_{x,wr}$ and δ can have significant differences in their magnitude, so scaling them by dividing each signal by its maximum value puts them at the same level and makes them of the same weight in the cost function. The importance of each signal can then be varied with a second weighting factor. The two other weighting functions W_δ and W_M are defined as follows:

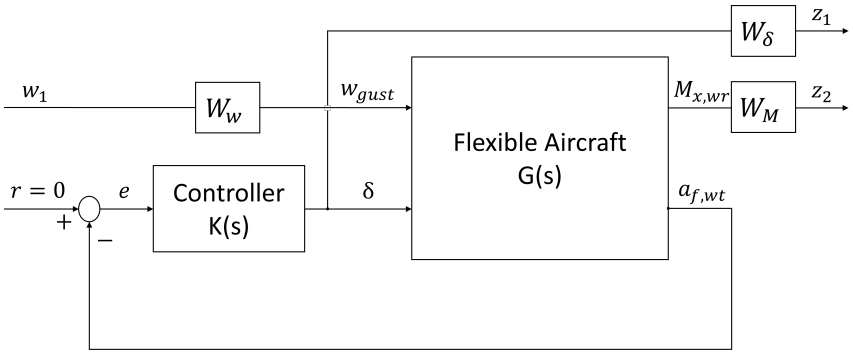

Fig. 4 Block diagram of the GLA synthesis setup.

$$W_\delta = f_\delta \frac{1}{\delta_{\max}} \qquad W_M = f_M \frac{1}{M_{x,wr\,\max}} \tag{16}$$

where δ_{max} and $M_{x,wr_{max}}$ are the maximum possible values of δ and $M_{x,wr}$, respectively. f_δ and f_M are weighting factors that can be tuned by the designer to achieve the desired results, and usually have an initial value of one. The regulated output signal z now has the following form:

$$\vec{z} = \begin{bmatrix} W_\delta\ \delta \\ W_M\ M_{x,wr} \end{bmatrix} \ . \tag{17}$$

Using equation 13, the GLA optimization problem can be formulated as follows:

$$\begin{aligned} &\min_K \|F_l(P,K)(s)\|_\infty \\ &\qquad \Updownarrow \ \|w\|_2 = 1 \\ &\min_K \max_\omega \left(\sqrt{|W_\delta \delta(j\omega)|^2 + |W_M M_{x,wr}(j\omega)|^2} \right) \ . \end{aligned} \tag{18}$$

Here, the infinity norm of $\|F_l(P,K)(s)\|_\infty$ is defined as the sum of the squared weighted Bode diagrams from w_{gust} to $M_{x,wr}$ and from w_{gust} to δ. To obtain the optimal GLA controller, the maximum value of this sum over all frequencies is minimized. Using the MATLAB function "hinfsyn" from the Robust Control Toolbox, the optimization problem is solved and the sought state-space GLA controller is calculated (A,B,C and D matrices).

The optimization problem defined in equation 18 aims to minimize both the control command δ and the bending moment $M_{x,wr}$. However, the physics of the GLA problem indicates that these are conflicting objectives and reducing one value leads to an increase in the other. The inclusion of the control command

δ in the cost function serves two primary purposes. First, it reduces the workloads on the actuator, leading to a longer lifetime and less maintenance needs. Second, it ensures that the control signals stay within the actuator limitations to avoid actuator saturation.

In fact, a good definition of the actuator's design requirements, which consider the GLA workloads, allows for the full use of it to alleviate gust loads. However, to ensure system stability, it is important to guarantee that the actuator limits are not exceeded. This is because the system stability analysis is based on the assumption that the system is linear. When the actuator is saturated, this assumption is violated, and the system is no longer linear.

Therefore, a better formulation of the objectives is to minimize the weight on the actuation effort such that the maximum deflection rate is reached to achieve the best load reduction of the bending moment. This can be accomplished primarily by tuning the weighting factors f_δ and f_M in an iterative process. Figure 5 shows the workflow of the GLA controller design process. Weighting factors only change the relative importance of each variable to the other, meaning that multiplying all factors by a constant does not change the optimization solution [33]. The problem is only scaled, but the minimum value, and hence the optimal solution, does not change in this case. Since the regulated output z has two components, changing only one weighting factor is sufficient to alter the relative importance of the two variables to each other. This simplifies the tuning process as only one weighting factor needs to be adjusted. For the GLA control law design, the weighting factor f_δ was tuned to achieve the optimization objective. The tuning process was performed manually and is based on a root-finding numerical algorithm called the bisection method [39, 40]. The final value found for f_δ was 1.15, with a maximum deflection rate of $\dot{\delta}_{\max} = 39.7°/\mathrm{s}$.

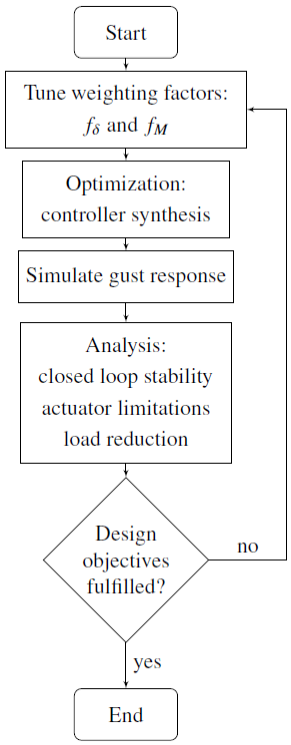

Fig. 5 Controller design workflow

3.3 Stability Analysis

In every modeling process, assumptions and simplifications are made, which can result in modeling errors. These errors are typically represented in the system as gain and phase uncertainties. To account for these errors in the stability analysis, it is important to have gain and phase margins to ensure the stability of the controller. As illustrated in table 3, the phase and gain margins of the closed-loop system are higher than the design requirements. In the Bode diagram of the open loop, the magnitude does not cross the zero line, indicating that the closed loop has an infinite phase margin.

Stability margins	Closed loop	Requirements
Gain margin	17.7 dB	7 dB
Phase margin	∞	60°

Table 3 Stability margins of the closed loop

This stability analysis can be interpreted that the system can have a gain error of any value until 17.7 dB, and the system will always be stable, regardless of how much delay the system has. However, this statement is not entirely accurate, since the definition of gain and phase margin is based on an individual consideration of gain and phase errors. Which means the system will be stable with a gain error less than 17.7 dB in case that the phase error is zero. However, if the phase error is not zero the real gain margin of the system with the combined error can be much less than the classical gain margin value. To address the limitations of this separate consideration of phase and gain margins, the stability of the system regarding simultaneous uncertainties is evaluated using the Nichols diagram [41], as illustrated in Figure 6.

To investigate the stability of the closed-loop system further, simultaneous uncertainties in gain and phase are added to the system. In [5], the following uncertainties are used: gain uncertainty: ±4 dB, Phase uncertainty: ±30°. Generally, in order to assess the stability of the system in the presence of these uncertainties, Monte-Carlo simulations can be performed, where all different combinations of gain and phase errors are examined [42]. Alternatively, the worst-case combination of gain and phase errors can be considered using disk margins [43, 44]. Since applying these methods exceeds the defined time frame of this work, a simpler approach is presented here for the particular case represented in Figure 6.

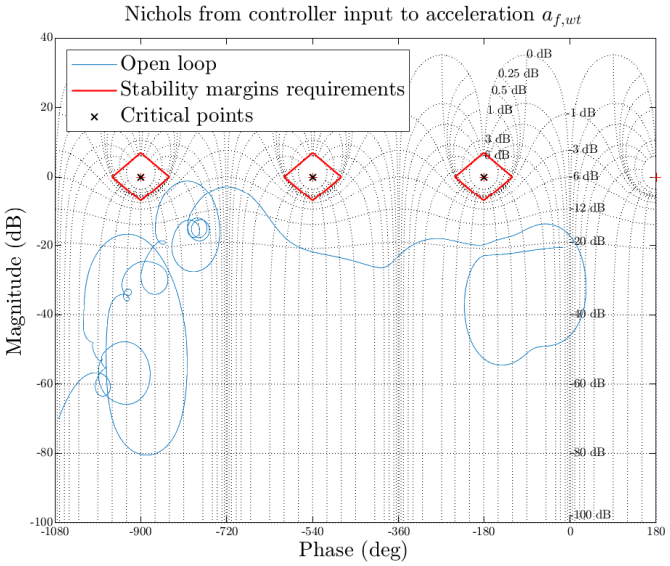

Fig. 6 Nichols diagram of the open loop

As shown in Figure 6, the nearest critical point to the open-loop curve, at which the system becomes unstable, is the black point on the left (-900,0). Gain errors represent a vertical shift of the curve in the Nichols diagram, while phase errors represent a horizontal shift. The worst-case combination of uncertainties (gain: ±4 dB, Phase: ±30°) is obtained at a positive gain error of 4 dB and a negative phase error of -30° (green dashed curve in Figure 7). These uncertainties are applied to the system by multiplying the open loop with the following transfer function $G(s)_{\text{uncertain}} = 4dB \cdot e^{\pi/180(-30°)i}$. As illustrated in Figure 7, the system with worst-case uncertainties is stable but has less stability margin than the unperturbed system. This demonstrates that the system is stable for any combination of ±4 dB gain and ±30° phase of simultaneous errors, with a robust stability margin of 6 dB gain and 24° phase.

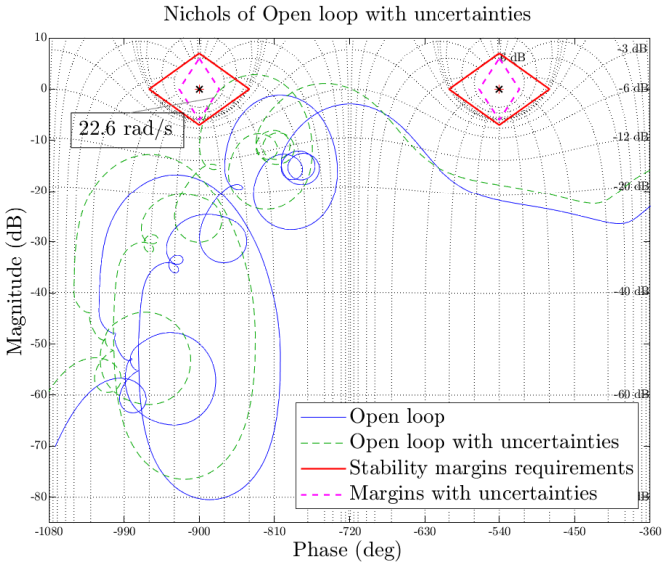

Fig. 7 Nichols diagram of the open loop with uncertainties

4 Simulation and Results

This section evaluates the designed GLA controller using closed-loop responses in the frequency and time domain. The primary focus is to validate the GLA controller with respect to its design requirements. The test cases consist of vertical discrete gusts with different gradients, as shown in Table 2. Additionally, the effectiveness of the current control strategy is assessed. Simulations are performed using the linear Flexible Aircraft Model (FAM) with a fixed time step of 0.005 seconds. The loads shown in this section are normalized using their steady-state values at the operating point.

4.1 Actuation Effort

One objective of the design is to limit the commanded control deflection and deflection rate to the maximum rate which can be achieved by the actuator. The limits of the actuator model are presented in table 1. The simulation results have shown that the deflection angle limit is not a critical aspect compared to the deflection rate limit (The maximum deflection angle is 3.27°). Figure 8 shows the real deflection rate of the control surfaces. It is clear that the tuning process described in Figure 5 has successfully achieved the objective of keeping the maximum deflection rate (39.71°/s) under the limit but very close to it. The maximum deflection rate occurs due to a discrete gust with H= 37 m, which is not as critical with respect to the wing root bending moment as the most critical discrete gust with H= 83 m. It would be advantageous in terms of load reduction to have the maximum deflection rate occur at the critical gust and let the actuator go into saturation for non-critical gusts, as the maximum deflection rate is the limiting factor for load reduction performance. However, the system stability cannot be guaranteed in this scenario.Therefore, it is necessary to tune the maximum deflection rate considering all relevant design cases.

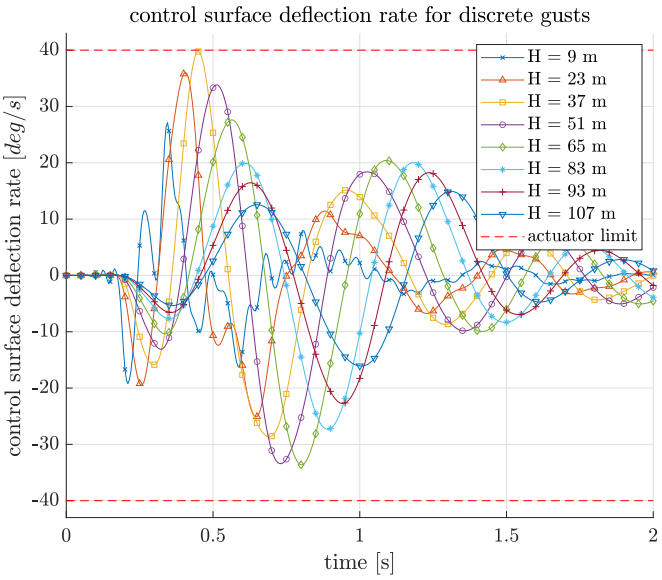

Fig. 8 Control surface deflection rate for discrete gusts.

4.2 Load Alleviation

In this section, the performance of the GLA controller is evaluated using closed-loop responses in both the frequency and time domains. To simplify the representation of data, consistent rules are used in all figures that illustrate data for multiple gust gradients. The green color represents the response without control, while the blue color represents the response with active control. Each gust gradient has a single marker for both responses (with and without control), such as '$*$' for H= 83 m. Therefore, only the entries for active control are displayed in the legend.

To evaluate the load reduction performance in the frequency domain, the closed loop transfer function from gust disturbance w_{gust} to wing root bending moment $M_{x,wr}$ is considered. Figure 9 shows the Bode diagram of the closed loop frequency response compared to the FAM response without controller. The effect of H_∞ optimal control design can be clearly seen in the reduced magnitude near 10 rad/s. The peak at this frequency corresponds to the first bending mode of the wing, and has been reduced from 173 dB (FAM) to 168 dB (Closed loop), indicating a reduction in wing root load of the first bending mode.

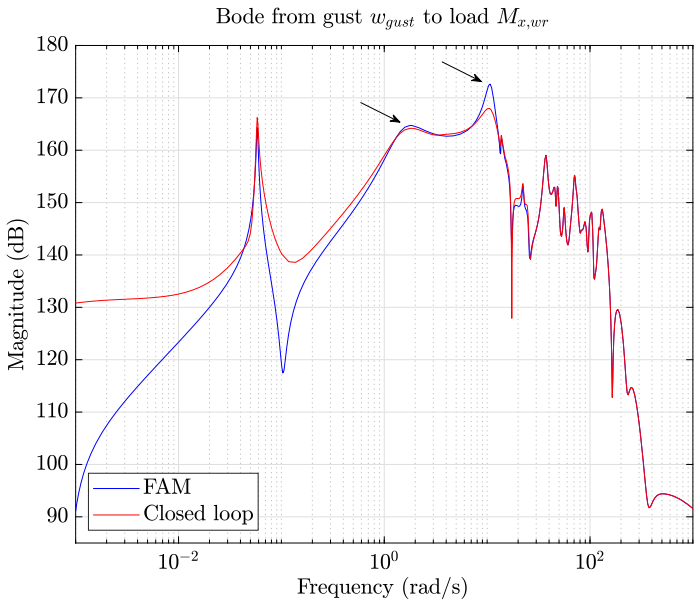

Fig. 9 Bode diagram from gust velocity w_{gust} to wing root bending moment $M_{x,wr}$

The Flexible Aircraft Model (FAM) response is simulated for all gust gradients defined in Table 2, and the wing root bending and torsion moment response are recorded. The same simulations are performed for the FAM with the GLA controller, and both results are compared to each other. Figure 10 shows the wing root bending and torsion moments for various discrete gusts. The reduction in the torsion moment load is only a positive physical consequence of reducing the bending moment load and was not explicitly included as a design objective or in the optimization process. This can be explained by the fact that the additional bending moment induced by the gust is physically linked to an accompanying torsion moment, as both are produced by the same additional lift force resulting from the gust [45]. Therefore, the reduction in lift force achieved by the GLA controller results in a reduction of both the bending and torsion moments.

In the left plot it can be observed that, there is a slight load reduction in the maximum load of the normalized bending moment, and the following load oscillations are significantly reduced with increased damping. Load oscillations are generally unwanted, as load cycles increase the risk of having a fatigue failure, even if the cycle amplitude does not exceed the ultimate strength of the material [2]. The controller has a positive effect regarding this aspect. As structure design requires the consideration of the combined load of bending and torsion moments [46], it is important to examine the reduction of the combined loads. Figure 10b shows the boundary of the bending and torsion moments with and without GLA controller. As illustrated, using the GLA controller, the area of the biggest boundary line has been reduced as well as the maximum combined values.

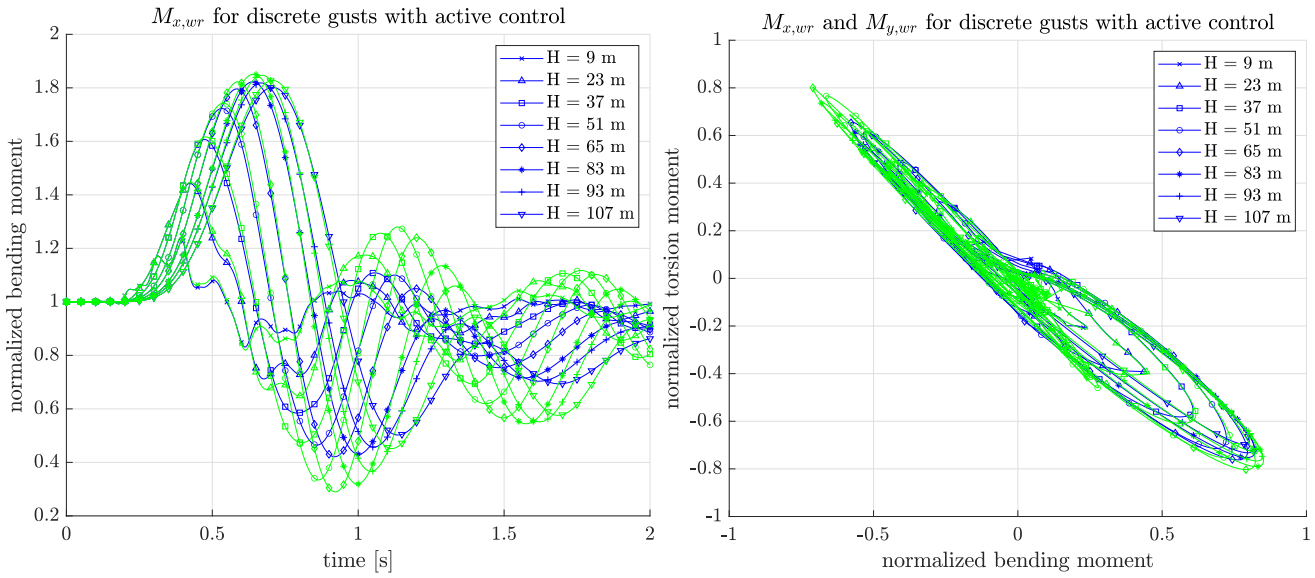

(a) Bending moment **(b) Bending and torsion moment**

Fig. 10 Simulation results for different gust gradients with(blue) and without control(green)

To evaluate the performance of this GLA controller the ratio between the maximum additional wing root bending moment without control $\Delta M_{x,wr}$=0.84 at H=83 m, and the new maximum additional load with control are considered. The total load reduction index P_{M_x} is defined as follows:

$$P_{M_x} = 100 \cdot \left(1 - \frac{\max\limits_{\forall H} \left(\max \left(\left| \Delta M_{x,wr,Cont} \right| \right) \right)}{\max\limits_{\forall H} \left(\max \left(\left| \Delta M_{x,wr} \right| \right) \right)} \right) . \tag{19}$$

Here, "$\max\limits_{\forall H} \left(\max \left(\left| \Delta M_{x,wr} \right| \right) \right)$" denotes the maximum absolute difference between the wing root bending moment of all gust gradients and the steady state value, while "$\max\limits_{\forall H} \left(\max \left(\left| \Delta M_{x,wr,Cont} \right| \right) \right)$" represents the

same value with GLA control. The current GLA controller has a total load reduction performance of the wing root bending moment of P_{M_x}=3.42%.

4.3 Control Strategy Assessment

As seen in the last section the current GLA controller has a relative small load reduction performance, with a total load reduction index of P_{M_x}=3.42%. The main limiting factor for load reduction performance was found to be the deflection rate limit of the actuator, which typically equals 40°/s for transportation aircraft actuators [5], as mentioned in Section 4.1.

New control technologies have been investigated to enhance actuator dynamics for flight control [3, 11, 47–49]. In this section the potential load reduction performance is investigated, when having better actuators with higher deflection rate limits. To this end, a parameter study is performed, to better understand the relationship between load reduction performance and deflection rate limit. In this study, the deflection rate limit requirement is relaxed in the optimization process, defined in Section 3.2, using a relaxation factor λ. Specifically, the actuation weighting function W_δ is divided by the relaxation factor $\lambda > 1$, resulting in a relaxed weighting function $W_{\delta,\text{relaxed}}$ given by:

$$W_{\delta,\text{relaxed}} = \frac{W_\delta}{\lambda} \quad . \tag{20}$$

Setting $\lambda > 1$ reduces the weighting factor of the actuator effort in the optimization process, allowing for higher deflection rates. The choice of the λ values is arbitrary since there is no concrete actuator rate value for which the GLA controller is designed. Using a relaxation factor of $\lambda = 2$, the maximum new deflection rate limit reached in this case is approximately 90°/s. With the higher deflection rate limit of 90°/s, the GLA controller is capable of reducing loads more effectively. Figure 11 displays the results of the wing root bending moment simulation obtained using this GLA controller. The load reduction performance is improved, with a total value of $P_{M_x} = 7.89\%$.

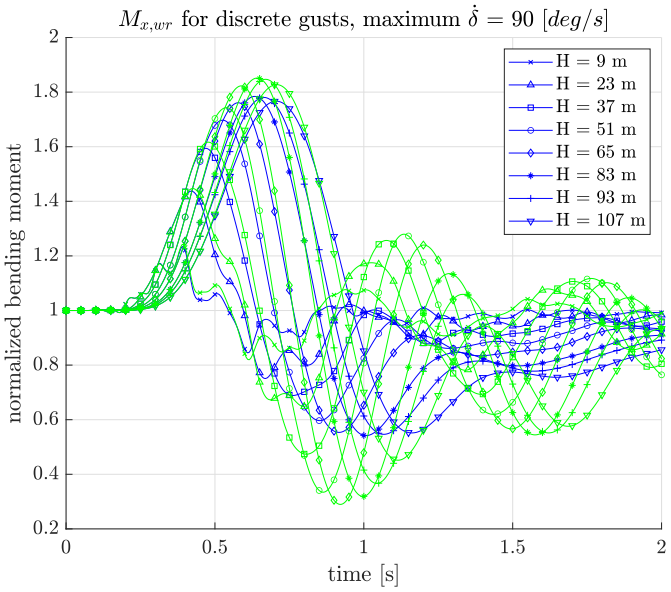

Fig. 11 $M_{x,wr}$ **with(blue) and without control(green), maximum deflection rate** $< 90°/s$

As expected, load reduction improves when using an actuator with a higher deflection rate. However, it is worth investigating whether there are other limiting factors in addition to the deflection rate. To explore this possibility, the relaxation factor is set to a very high value ($\lambda = 10^3$) to eliminate the deflection rate constraint. The simulation results of this case, with a maximum deflection rate of $\dot{\delta}_{\max} = 3380°/s$, shows that the controller has reached a total load reduction value of only $P_{M_x} = 30.57\%$, even with this unrealistic high deflection rate.

To understand these surprising results, a parameter study was conducted, in which the total load reduction was represented as a function of the maximum actuator deflection rate, using different values for $\lambda > 1$. The study was performed using the following λ values: (1, 2, 5, 10, 20, 40, 1000). The results for λ=1 represent the initial GLA controller design. Figure 12 shows the total load reduction P_{M_x} for wing root bending moment as a function of the maximum deflection rate $\dot{\delta}_{max}$. As shown in Figure 12, the potential benefits of increasing the deflection rate limit are high at the beginning ($P_{M_x} = 16\%$ & 21% for $\dot{\delta}_{\max} = 171°/s$ & $245°/s$), but the curve converges to a boundary value at high deflection

rates, indicating that the benefit is limited. This limit value can be predicted by fitting a rational curve, as shown in Figure 12. The curve converges to a maximum value of the total load reduction, indicating that even with an infinite deflection rate of the actuator, it is expected that the total load reduction will not exceed 33%. This limitation can be attributed to the used control strategy, where the GLA controller waits for the wing tip to move before attempting to counteract these movements, and this strategy has inherent physical limitations.

To assess the current control strategy, a comparison to another control approach presented in [5] is performed, to classify its load reduction performance. The approach in [5] uses H_∞ optimal control to design a GLA controller for a commercial aircraft concept. Ailerons and elevator are utilized as control surfaces, while Lidar, gyroscopes, accelerometers, and alpha-probe serve as sensors. Results in [5] reveal that a non-robust controller can achieve a wing root load reduction of up to 72%, 57% with the same robustness as used here, and 22% without Lidar. These results emphasize the importance of the chosen control strategy and the ability to predict wind gusts before they reach the aircraft wing. They indicate that predicting disturbances represents the second limiting factor in increasing load reduction performance.

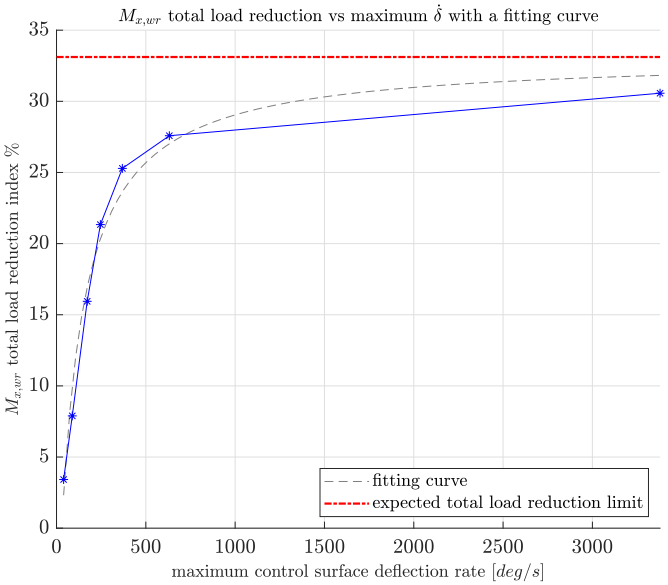

Fig. 12 Predicted total load reduction P_{M_x} limit using a rational fitting curve

5 Conclusion

This work establishes a framework for designing a control law for gust load alleviation (GLA) of a flexible aircraft equipped with acceleration sensors. The focus of the control law design is on alleviating bending moment loads at the wing root using one accelerometer. A full-order state-space GLA controller has been designed using classical H_∞ optimal control. The optimization process seeks to minimize wing root bending moment and actuator effort. A stability analysis has been performed, ensuring that the system's design stability margins are guaranteed (gain: 7 dB, phase: 60°). To assess the controller's robustness, combined system uncertainties of 4 dB gain and 30 degrees phase have been considered. The worst-case combination of these uncertainties results in a robust stability margin of 6 dB gain margin and 24 degrees phase margin.

The controller's load alleviation performance was tested using vertical gusts with variable gust gradients. The simulations demonstrate that the actuator deflection rate limit is the limiting factor for performance. The results indicated a reduction in the maximum wing root bending moment of 3.4%, with a maximum deflection rate of 40°/s. By relaxing the actuator effort condition in the optimization process, higher load reduction values can be achieved. For instance, a load reduction of 7.9% has been attained using a maximum deflection rate of 90°/s. A parameter study was conducted to investigate the relationship between load reduction and deflection rate. The study showed that the load reduction performance converges to a value of approximately 33% as the deflection rate increases towards infinity. This is due to the fact that the feedback strategy with sensors on the wing has limited performance; it waits until the wing moves, then sends a control signal to counteract the gust effect.

For future work, the control design framework can be easily extended to include additional sensor types and control signals since it is based on a full-order state-space controller. The four outboard

ailerons can be operated separately, in addition to the elevator, enabling the inclusion of more loads, such as bending moment and shear force, in the optimization process [5]. The feedback signals can be expanded to include more sensors to capture wind gusts before they reach the aircraft wing.

Acknowledgments

This study was funded by the German Aerospace Center in Oberpfaffenhofen. The given support is greatly appreciated.

References

[1] Minwoo LEE, Larry K.B. LI, and Wenbin SONG. Analysis of direct operating cost of wide-body passenger aircraft: A parametric study based on hong kong. *Chinese Journal of Aeronautics*, 32:1222–1243, 5 2019. ISSN: 10009361. DOI: 10.1016/j.cja.2019.03.011.

[2] Jan R Wright and Jonathan E Cooper. *Introduction to Aircraft Aeroelasticity and Loads Aerospace*. Wiley, 2 edition, 2014. ISBN: 978-1-118-48801-0.

[3] Yonghong Li and Ning Qin. A review of flow control for gust load alleviation. *Applied Sciences (Switzerland)*, 12, 10 2022. ISSN: 20763417. DOI: 10.3390/app122010537.

[4] Shijun Guo, Jaime Espinosa De Los Monteros, and Ying Liu. Gust alleviation of a large aircraft with a passive twist wingtip. *Aerospace*, 2:135–154, 6 2015. ISSN: 22264310. DOI: 10.3390/aerospace2020135.

[5] Hugo Fournier, Paolo Massioni, Minh Tu Pham, Laurent Bako, Robin Vernay, and Michele Colombo. Robust gust load alleviation of flexible aircraft equipped with lidar. *Journal of Guidance, Control, and Dynamics*, 45:58–72, 1 2022. ISSN: 15333884. DOI: 10.2514/1.G006084.

[6] Jia Xu. *Aircraft Design With Active Load Alleviation and Natural Laminar Flow*. PhD thesis, Stanford University, 2012. `http://purl.stanford.edu/hz528zb1688`.

[7] T. E. Disney. C-5a active load alleviation system. *Journal of Spacecraft and Rockets*, 14:81–86, 1977. ISSN: 00224650. DOI: 10.2514/3.57164.

[8] J. F. Johnston. Accelerated development and flight evaluation of active controls concepts for subsonic transport aircraft. volume 1: Load alleviation/extended span development and flight tests. Technical Report LR 29003-1; NASA-CR-159097, Lockheed-California (under NAS1-14690), 1979. `https://ntrs.nasa.gov/citations/198200072030`.

[9] Sensburg O, Becker J, Lusebrink H, and Weiss F (ICAS-82-2.1.1). Gust load alleviation on Airbus A300. In *13th Congress of the International Council of the Aeronautical Sciences*, 1982.

[10] B.W. Payne. Designing a load alleviation system for a modern civil aircraft (icas-86-5.2.3). In *15th Congress of the International Council of the Aeronautical Sciences*, 9 1986.

[11] Nader Al-Battal. *Flow Control for Loads Control 2018*. PhD thesis, University of Bath, 2018.

[12] Nikolaus P. Schmitt, Wolfgang Rehm, Paul Zeller, Thomas Pistner, Guenther Reithmeier, Stephan Stilkerich, Hermann Diehl, Klaus Schertler, and Helmut Zinner. The awiator airborne lidar turbulence sensor. *CLEO/Europe. Conference on Lasers and Electro-Optics Europe*, page 448, 2005. DOI: 10.1109/CLEOE.2005.1568226.

[13] N. P. Schmitt, W. Rehm, T. Pistner, H. Diehl, P. Nave, G. Jenaro-Rabadan, P. Mirand, and M. Reymond. Flight test of the awiator airborne lidar turbulence sensor. In *14th Coherent Laser Radar Conference*, 7 2007. ISBN: 9781615671557.

[14] N P Schmitt, W Rehm, T Pistner, H Diehl, P Navé, and G Jenaro Rabadan. A340 flight test results of a direct detection onboard UV Lidar in forward looking turbulence measurement configuration. Technical report, EADS, 2009.

[15] Ahmed Khalil and Nicolas Fezans. Performance enhancement of gust load alleviation systems for flexible aircraft using h_∞ optimal control with preview. In *AIAA Scitech 2019 Forum*. American Institute of Aeronautics and Astronautics Inc, AIAA, 2019. ISBN: 9781624105784. DOI: 10.2514/6.2019-0822.

[16] Jie Zeng, Boris Moulin, Raymond De Callafon, and Martin J. Brenner. Adaptive feedforward control for gust load alleviation. *Journal of Guidance, Control, and Dynamics*, 33:862–872, 2010. ISSN: 15333884. DOI: 10.2514/1.46091.

[17] Christopher D Regan and Christine V Jutte. Survey of applications of active control technology for gust alleviation and new challenges for lighter-weight aircraft. Technical Report TM—2012–216008, NASA, 2012.

[18] Federico Fonte, Sergio Ricci, and Paolo Mantegazza. Gust load alleviation for a regional aircraft through a static output feedback. *Journal of Aircraft*, 52:1559–1574, 2015. ISSN: 15333868. DOI: 10.2514/1.C032995.

[19] Susan A. Frost, Brian R. Taylor, and Marc Bodson. Investigation of optimal control allocation for gust load alleviation in flight control. In *AIAA Atmospheric Flight Mechanics Conference*, 2012. ISBN: 9781624101847. DOI: 10.2514/6.2012-4858.

[20] Mayuresh J. Patil and Dewey H. Hodges. Output feedback control of the nonlinear aeroelastic response of a slender wing. *Journal of Guidance, Control, and Dynamics*, 25:302–308, 2002. ISSN: 07315090. DOI: 10.2514/2.4882.

[21] Andreas Wildschek, Rudolf Maier, Falk Hoffmann, Matthieu Jeanneau, and Horst Baier. Active wing load alleviation with an adaptive feedforward control algorithm. *Collection of Technical Papers - AIAA Guidance, Navigation, and Control Conference*, 1:237–257, 2006. DOI: 10.2514/6.2006-6054.

[22] Mushfiqul Alam, Martin Hromcik, and Tomas Hanis. Active gust load alleviation system for flexible aircraft: Mixed feedforward/feedback approach. *Aerospace Science and Technology*, 41:122–133, 2015. ISSN: 12709638. DOI: 10.1016/j.ast.2014.12.020.

[23] Nicolas Fezans and Hans-Dieter Joos. Combined feedback and lidar-based feedforward active load alleviation. In *AIAA Atmospheric Flight Mechanics Conference*. American Institute of Aeronautics and Astronautics (AIAA), 6 2017. DOI: 10.2514/6.2017-3548.

[24] Christian Reschke. *Integrated Flight Loads Modelling and Analysis for Flexible Transport Aircraft*. PhD thesis, Institute of Flight Mechanics and Controls, University of Stuttgart, German Aerospace Center DLR, July 2006. DOI: 10.18419/opus-3733.

[25] Thiemo Kier and J Hofstee. Varloads eine simulationsumgebung zur lastenberechnung eines voll flexiblen, freifliegenden flugzeugs. In *Deutscher Luft- und Raumfahrtkongress*, 2004. `https://www.researchgate.net/publication/224782818`.

[26] Thiemo M Kier and Gertjan H N Looye. Unifying manoeuvre and gust loads analysis models. In *International Forum on Aeroelasticity and Structural Dynamics IFASD-2009-106*, 2009. `https://elib.dlr.de/97798/1/IFASD-2009-106.pdf`.

[27] Simon Schulz and Daniel Ossmann. Estimation of global structural aircraft loads due to atmospheric disturbances for structural fatigue estimation. *International Forum on Aeroelasticity and Structural Dynamics, Spain*, 2022.

[28] W.P. Rodden, J.P. Giesing, and T.P. Kalman. New developments and applications f the subsonic doublet-lattice method for nonplanar configurations, agard. *Symposium of Unsteady Aerodynamics for Aeroelastic Analyses of Interfering Surfaces AGARD-CP-80-71. AGARD*, 1971.

[29] Edward Albano and William P. Hodden. A doublet-lattice method for calculating lift distributions on oscillating surfaces in subsonic flows. *AIAAJ*, 7:279–285, 1969. ISSN: 0001-1452. DOI: 10.2514/3.5086.

[30] European Aviation Safety Agency (EASA). Certification specifications for large aeroplanes CS-25. Technical report, 2007.

[31] S Skogestad and I Postlethwaite. *Multivariable Feedback Control - Analysis and Design - Second Edition*. Wiley, 2005. ISBN: 13 978-0-470-01167-6.

[32] SAE International. Vehicle management systems - flight control function, design, installation and test of piloted military aircraft. Technical report, 2018. `https://www.sae.org/standards/content/as94900a/`.

[33] Thivaharan Albin Rajasingham. *Nonlinear Model Predictive Control of Combustion Engines*. Springer Cham, 2021. ISBN: 978-3-030-68010-7.

[34] John C. Doyle, Keith Glover, Pramod P. Khargonekar, and Bruce A. Francis. State-space solutions to standard h_2 and h_∞ control problems. *IEEE Transactions on Automatic Control*, 34:831–847, 1989. ISSN: 15582523. DOI: 10.1109/9.29425.

[35] Diego Navarro Tapia. *Robust and Adaptive TVC Control Design Approaches for the VEGA Launcher*. PhD thesis, University of Bristol, 2019.

[36] Stephen P. Boyd and Lieven Vandenberghe. *Convex Optimization*. Cambridge University Press, 2004. ISBN: 9780521833783.

[37] Pascal Gahinet and Pierre Apkarian. A linear matrix inequality approach to h_∞ control. *International Journal of Robust and Nonlinear Control*, 4:421–448, 1994. ISSN: 10991239. DOI: 10.1002/rnc.4590040403.

[38] Abdelmoez Elagroudy. Flight control law design for gust load alleviation of flexible aircraft using extended gust modeling. Master's thesis, Institute of Flight System Dynamics, RWTH Aachen, German Aerospace Center DLR, Oberpfaffenhofen, Mar. 2023. DOI: 10.13140/RG.2.2.25550.88643.

[39] Claus-Dieter Munz and Thomas Westermann. *Numerische Behandlung Gewöhnlicher und Partieller Differenzialgleichungen*. Springer, 2019. ISBN: 978-3-662-55886-7.

[40] Richard L. Burden and J. Douglas Faires. *Numerical Analysis*. Cengage Learning, 2010. ISBN: 9780538733519.

[41] Jacqueline Wilkie, Michael Johnson, and Reza Katebi. Analysis and simple design using the nichols chart. *Control Engineering*, pages 505–528, 2002. DOI: 10.1007/978-1-4039-1457-6_17.

[42] Laura Ryan Ray and Robert F. Stengel. A Monte Carlo approach to the analysis of control system robustness. *Automatica*, 29:229–236, 1 1993. ISSN: 0005-1098. DOI: 10.1016/0005-1098(93)90187-X.

[43] Pasala Gopi, Suresh Srinivasan, and Murugaperumal Krishnamoorthy. Disk margin based robust stability analysis of a dc motor drive. *Engineering Science and Technology, an International Journal*, 32, 8 2022. ISSN: 22150986. DOI: 10.1016/j.jestch.2021.10.006.

[44] Richard Tymerski. Worst case stability analysis of switching regulators using the structured singular value. *IEEE Workshop on Computers in Power Electronics*, pages 105–112, 1996. ISSN: 10935142. DOI: 10.1109/PESC.1994.349720.

[45] T. H.G. Megson. *Aircraft Structures for Engineering Students*. Elsevier, 2021. ISBN: 9780128228685.

[46] Walter D. Pilkey, Zhuming Bi, and Deborah F. Pilkey. *Peterson's stress concentration factors*. Wiley, 2020. ISBN: 978-1-119-53252-1.

[47] Dale Berg, Scott J Johnson, C P Case, and Van Dam. Active load control techniques for wind turbines. Technical report, Sandia National Laboratories, 2008. DOI: 10.2172/943932.

[48] Scott J. Johnson, Jonathon P. Baker, C. P. Van Dam, and Dale Berg. An overview of active load control techniques for wind turbines with an emphasis on microtabs. *Wind Energy*, 13:239–253, 2010. ISSN: 10991824. DOI: 10.1002/we.356.

[49] Yonghong Li. *Gust Load Alleviation by Fluidic Actuators on a Blended-Wing-Body Configuration*. PhD thesis, University of Sheffield, 2020.